Journal of Manufacturing Science and Engineering. Received May 18, 2020;
Accepted manuscript posted May 20, 2020. doi:10.1115/1.4048378

Mechanical and Corrosion Assessment of Friction Self-piercing rivet joint of carbon fiber-reinforced polymer and magnesium alloy AZ31B

Yong Chae Lim*, Jian Chen, Jiheon Jun, Donovan N. Leonard, Michael P. Brady, Charles David Warren, and Zhili Feng

Materials Science & Technology Division, Oak Ridge National Laboratory
One Bethel Valley Road, Oak Ridge, TN 37831, USA
(limy@ornl.gov, chenj@ornl.gov, junj@ornl.gov, leonarddn@ornl.gov, bradymp@ornl.gov, warrencd@ornl.gov, fengz@ornl.gov)

*Contact author: Dr. Yong Chae Lim (limy@ornl.gov)
Tel: +1-865-574-4805
Address: One Bethel Valley Road, Oak Ridge, TN 37831, USA

Keywords: dissimilar material joining; carbon fiber reinforced polymer; AZ31B; friction self-piercing riveting; mechanical strength; corrosion performance

ABSTRACT

In the present work, thermoset carbon fiber–reinforced polymer (CFRP) was spot joined to magnesium alloy AZ31B by a friction self-piercing riveting (F-SPR) process. Lap shear tensile and cross-tension testing were used to evaluate the mechanical joint performance. An average lap shear tensile load of 5.18 kN was achieved, while an average of 2.81 kN was found from cross-tension testing. All F-SPR samples showed pull-out of AZ31B after mechanical testing, indicating good mechanical interlocking between the steel rivet and AZ31B. Corrosion potential was measured for each material to establish the galvanic corrosion characteristics. As expected, AZ31B was found to be the most active, while thermoset CFRP was the most noble. The steel rivet fell between the AZ31B (active) and the thermoset CFRP (noble). Salt fog corrosion testing (ASTM B-117) was performed to evaluate the corrosion performance of the uncoated F-SPR joint. With up to 200 h of exposure, the post-corroded F-SPR joint integrity retained 81.2% of the pre-exposure F-SPR joint strength with AZ31B pull-out failure mode. From cross-sectional analysis of the F-SPR joint, extensive corrosion of AZ31B was observed at the joint and other exposure areas. However, steel rivet was not significantly corroded due to sacrificial anode effect by which AZ31B corroded first in the galvanic couple.

1. Introduction

Extensive research and development efforts have focused on the development of multi-material lightweight vehicles to improve fuel efficiency and reduce greenhouse gas emissions [1-4]. Currently, carbon fiber–reinforced composites, magnesium (Mg) alloys, high-strength aluminum (Al) alloys, and advanced or ultrahigh-strength steels have been identified as feasible lightweight materials for body and closure multi-material lightweight vehicle components [3]. Among the four candidate materials, Mg alloys have the highest specific strength (i.e., strength divided by density) with a density of 1.8 g cm^{-3} and yield strength of up to 285 MPa [5]. Carbon fiber–reinforced composites, another type of low-density and high-strength material, are characterized by design flexibility and tailored mechanical properties [6,7]. Therefore, the integration of Mg alloys and carbon fiber composites into a unified vehicle structure can have a great impact on fuel efficiency improvement.

One critical challenge to the development of multi-material vehicles is how to join the physical and chemical dissimilarities of different materials, such as metals to polymer composites. Limited research has focused on joining metal to polymer composites by laser welding [8]; resistance spot welding with silane surface treatment [9]; solid-state [10-12], ultrasonic [13], and mechanical fastening [14]; and adhesive bonding and weld bonding [15]. Most previous studies considered how to weld or join Al alloys to thermoplastics or advanced ultrahigh-strength steels to thermoplastic polymers because of the nature of the different joining techniques (i.e., to form chemical bonding), excluding mechanical fastening. However, limited research has been conducted on joining carbon fiber–reinforced polymers (CFRP) to Mg alloys [16,17]. Two previous studies [16,17] used frictional heat from friction spot joining or conducted heat from a hot metal block (400–600°C) to chemically bond the thermoplastic (e.g., poly(phenylenesulfide)

or polyurethane) CFRP and the Mg alloy AZ31B at the joint interface. However, structural vehicle applications would require CFRPs of high strength and stiffness, such as thermoset carbon fiber composites. The strength of thermoplastic polymers is known to be less than that of thermoset composites. They are not as strong because thermosets have a network of strong covalent crosslinks compared with the flexible chains found in thermoplastics. Therefore, neither of the previous methods (i.e., frictional spot joining or hot metal pressing) used to form chemical bonding at joint interfaces can be easily applied to join thermoset CFRPs to metals because thermoset plastics do not melt after being fully hardened (i.e., it does not crosslink). Therefore, one objective of the present work is to join thermoset CFRPs to an Mg alloy sheet.

The next critical concern was to join the Mg alloy AZ31B and thermoset CFRP at room temperature by mechanical fastening, such as self-piercing riveting (SPR), but Mg is characterized by low ductility and formability due to three slip systems in the lattice structure [18]. To overcome this challenge, AZ31B was preheated to temperatures ranging from 150 to 200°C by induction heating [19], laser [20], and an electrically heated plate [21] prior to SPR. Cracking of AZ31B after joining was greatly minimized, which led to improved mechanical joint strength. However, auxiliary heating equipment can result in increased joining time and cost. Recently, a unique spot joining process, friction self-piercing rivet (F-SPR), was proposed [22,23]. This method uses frictional heat from friction stirring and mechanical interlocking from SPR. Essentially, the rivet rotates while being plunged into the workpiece, and local frictional heat is generated when the rivet interacts with the surrounding metal workpiece. This additional frictional heat improves the local ductility of the AZ31B sheet to effectively avoid cracking. For this reason, the authors employed F-SPR to join thermoset CFRP to AZ31B.

Another critical concern when joining dissimilar materials is joint strength/performance under corrosive environments. Thus, the corrosion behavior of joints formed from dissimilar materials should be thoroughly assessed before any such materials can be used in automotive body structures. It is critical to consider both the joining process and corrosion behavior of dissimilar joints [24-27]. These previous works studied the corrosion of Al alloys (6xxx or 7xxx)–steel joints, Al alloy–glass fiber composite joints, and Mg alloy–glass fiber composite joints by cyclic corrosion or environmental cycling testing. The joint strength of dissimilar materials was greatly reduced without proper corrosion protection. Mg is a highly active metal in the galvanic series [28], so for F-SPR joining of an Mg alloy with a CFRP, galvanic corrosion of AZ31B in contact with the steel rivet and the thermoset CFRP can be a great concern, and coatings or surface treatments will be needed.

In the present work, F-SPR was employed to develop a joining technique for dissimilar materials by combining thermoset CFRP and AZ31B. Then, tensile shear and cross-tension testing were conducted to evaluate the integrity of the F-SPR joints. The corrosion potential of AZ31B, thermoset CFRP, steel rivet, and graphite rod was measured to determine their respective positions in galvanic series. Then, F-SPR joint strength was studied after ASTM B-117 salt fog corrosion exposure testing. Lap shear tensile testing was conducted to study joint strength for post-corroded samples. Cross-sectional analysis of post-corroded F-SPR specimens with different exposure times was performed using optical and scanning electron microscopy (SEM) coupled with energy dispersive spectroscopy.

2. Materials and Methods

2.1 Materials

For the top sheet material, a 1.86 mm thick thermoset CFRP (Clearwater Composites, Minnesota, USA) was used. The composite was made with the G-83 prepreg (T700, Toray) in a 0°/90°, unidirectional, 9-ply layup. For the bottom sheet, a commercially available 2.36 mm thick Mg alloy AZ31B sheet was used. Japanese Industrial Standard G3507-2 carbon steel (SWCH18A) was used for the fabrication of the steel rivet. A hexagonal profile 9.525 mm in width was designed as a rivet head to be externally driven by the rivet holder during joining. Rivet shank diameter and leg length were 5.3 mm and 6 mm, respectively. Pip die, which has been widely used in self-piercing riveting, was employed. A schematic and dimensions of the rivet and pip die are provided in Figure 1. Chemical compositions of the AZ31B sheet and steel rivet were analyzed at IMR Test Labs (Lansing, NY, USA) and are summarized in Table 1. Mechanical properties of each material are summarized in Table 2.

All sheet materials were cut into lap shear coupons (25.4 mm wide and 101.6 mm long) and cross-tension coupons (50 mm wide and 150 mm long), as illustrated in Figure 2. Isopropyl alcohol was used to clean the composite and acetone was used to clean the metal surfaces prior to joining.

2.2 Description of F-SPR and Joint Fabrication

A simple illustration of F-SPR is provided in Figure 3 based on the prior works [22,23]. First, the external driven rivet is rotated and plunged into a workpiece with downward axial force. Localized frictional heat is generated between the rivet and sheet metal, leading to improved local ductility of the bottom sheet material (e.g., AZ31B). Next, the rivet leg is flared out in the bottom sheet based on the supporting die geometry, creating mechanical interlocking in the workpiece. After

preliminary F-SPR experiments with the highest lap shear failure load and no cracking on the backside of the AZ31B, the process parameters were finalized and are summarized in Table 3. The same welding conditions were then applied to spot join cross-tension coupons.

2.3 Static Lap Shear Tensile and Cross-Tension Testing of F-SPR Specimens

To evaluate the joint strength of F-SPR coupons, both lap shear tensile and cross-tension testing were performed using an MTS Systems tensile machine with a constant crosshead speed of 10 mm/min at room temperature. For lap shear tensile testing, spacers were used to hold the lap shear coupons to align them vertically between the grips.

2.4 Corrosion Potential Measurement

The corrosion potentials (E_{corr}) of the AZ31B sheet, thermoset CFRP, steel rivet, and graphite rod were measured in 0.1 M NaCl solution open to air at room temperature using a reference saturated calomel electrode (SCE). The distance between the working electrode (e.g., AZ31B, thermoset CFRP, steel rivet, and graphite rod) and SCE was kept at approximately 20 mm during the corrosion potential measurement, as shown in Figure 4. The comparison of corrosion potentials can indicate if a material will act as a cathode or anode in a galvanic couple with another material.

2.5 Salt Fog Corrosion Testing of F-SPR Specimens

To assess the mechanical integrity of F-SPR joints after corrosion exposure, the lap shear specimens were exposed to salt fog as per ASTM B-117. The CFRP sides of the joint specimens were inserted in the slots of a horizontal Teflon bar. The angle between the inserted specimen and the bar was approximately 60°, as shown in Figure 5. The side of the F-SPR specimen that was directly exposed to the salt fog had a step between the CFRP and AZ31B at the joint section. A

total of six F-SPR samples were prepared for ASTM B-117 testing as an initial assessment (set#1). Because of the aggressive general corrosion of Mg alloys, the exposure time for the F-SPR specimens was initially intended to be only 24 h, 100 h, and 200 h. The joint strength of post-corroded F-SPR was assessed by lap shear tensile testing. After each exposure time, two samples were removed from the corrosion chamber, rinsed thoroughly with running 4 Mohm·cm-grade water, and dried with compressed air. An additional two sample sets (i.e., #2 and #3) were conducted to assess the statistical variation in the sample behavior. The results of lap shear tensile testing were used to evaluate the joint integrity. Selected post-exposure specimens were mounted in epoxy to characterize cross-sectioned F-SPR joints after corrosion.

2.6 Metallurgical Characterization

To characterize the joint interface between the rivet and workpiece, selected F-SPR samples were cross sectioned, mounted, and polished for metallographic examination using standard metallographic techniques. Then, an optical microscope (Nikon Epiphot) and a scanning electron microscope (Hitachi S4800) coupled with an energy dispersive spectroscopy (EDS) detector were used. Accelerator voltage ranged from 10 to 15 kV for SEM images and element mapping on the joint area.

3. Results and Discussion

3.1. Mechanical Testing of F-SPR Specimens

Figure 6 depicts load versus displacement curves from lap shear tensile and cross-tension testing of F-SPR joints. For lap shear tensile testing, the average peak fracture load was 5.18 kN. Also, average absorbed energy as another joint property was calculated to be 26.05 J. For cross-tension testing, the average peak failure load and absorbed energy were found to be 2.81 kN and 17.91 J,

respectively. The peak failure load in lap shear tensile testing was mainly determined by the shear deformation of the rivet legs, which was related to the cross-sectional area of the joint and rivet length. However, the peak fracture load in cross-tension testing largely depended on the interlocking distance. For this reason, the peak load-bearing load and absorbed energy from the cross-tension testing were lower than the load and absorbed energy from the lap shear tensile testing. Table 4 summarizes peak lap shear failure load and absorbed energy for each tested sample. Representative fractographic images from mechanical testing of F-SPR joints are provided in Figure 7. From tensile shear testing, the rivet pulled out the bottom sheet of AZ31B (Figure 7[b]), indicating good mechanical interlocking between the rivet and the bottom sheet of AZ31B. All F-SPR joints showed the same failure mode from lap shear tensile testing.

Figure 8(a) shows a cross-sectional view of the as-formed F-SPR joint. No cracking of AZ31B was observed. Some characteristic dimensions were measured based on the SPR joint quality criteria [29]. Three major quality criteria are the rivet head height, the interlock distance, and the minimum remaining bottom material thickness. The rivet head height (the distance between the rivet head and the top sheet) was measured to be approximately −0.16 mm. This negative distance means that the rivet head is below the flush surface of the top CFRP sheet. The rivet head height is vital for several reasons, such as cosmetic appearance, tightness of the joints, and joint strength. Previous work reported that greater interlocking is achieved at a lower rivet head height [30]. Next, the interlock distance (amount of rivet flaring), which is related to mechanical interlocking between the rivet leg and workpiece, was measured to be 0.54 mm. This interlock distance is the most critical joint quality indicator because it dictates the locking strength between the rivet and the bottom sheet, as well as the load path during mechanical loading. Finally, the remaining bottom sheet thickness between the edge of the rivet leg and the bottom sheet was measured to be 0.13

mm. These measured dimensions are related to process conditions, as well as dimensions and configuration of die. Figure 8(b) shows magnified SEM image at the interface between the rivet head and CFRP. Carbon fibers are seen with different stacking sequences (0°/90°). Small microscale porosity and delamination are observed potentially due to compression and shear deformation of the fibers as well as compression of the composite matrix during the F-SPR process. Figure 8(c) shows at the interface between the rivet and the AZ31BB. Somewhat complex material mixing of AZ31B and CFRP because the rivet was rotated and plunged into the AZ31B. Some flash of AZ31B was partially plunged into the CFRP matrix. Also, some carbon fibers were imbedded into the AZ31B as a result of joining process.

3.2. Corrosion Potential Measurement of AZ31B, CFRP, Steel Rivet, and Graphite Rod

The corrosion potential of the individual materials provide insight into the extent of galvanic corrosion when the joint materials are in physical contact in the presence of a corrosive electrolyte. The corrosion potential of the AZ31B sheet, thermoset CFRP, steel rivet, and graphite rod were measured individually in 0.1 M NaCl at room temperature as a function of time and are plotted in Figure 9. Table 5 also summarizes the corrosion potential of each material. AZ31B exhibited a relatively steady corrosion potential of around –1.56 V_{SCE}, which agrees with other measurements from the literature [31-33]. The corrosion potential of the steel rivet began at around –0.47 V_{SCE} and shifted to below –0.6 V_{SCE}, which is common for a low-carbon steel [34]. The corrosion potential of the steel rivet was at least 0.9 V higher than that of AZ31B. The thermoset CFRP and graphite rod exhibited a corrosion potential greater than 0.1 V_{SCE} for the duration of the measurement and at least 0.57 and 1.66 V greater than the steel rivet and AZ31B sheet, respectively. The corrosion potential difference between graphite and CFRP narrowed and converged close to 0.2 V_{SCE}. The measured corrosion potential of CFRP was similar to the value (0.28 V_{SCE}) found in

the literature [35]. In summary, as expected, AZ31B was the most active material, while thermoset CFRP was the most noble material. The corrosion potential of the steel rivet was intermediate to that of the AZ31B and the thermoset CFRP.

3.3. Salt Fog Corrosion Testing of F-SPR Specimens

ASTM B-117 salt spray exposure is a widely used accelerated corrosion test for coated alloys and multi-material joints. In this work, uncoated F-SPR joints (where AZ31B would corrode significantly) were exposed to the salt spray to investigate the baseline corrosion damage. In service, such materials will require coatings or surface treatments. After 100 h and 200 h of exposure, uncoated F-SPR specimens exhibited massive corrosion of AZ31B (as expected), with the Mg dissolution more pronounced at the step of the CFRP and the AZ31B forming corrosion ditches as shown in Figure 10. Because of the loading direction of the F-SPR specimens, as shown in Figure 5(b), the step would be a likely area for the formation of stagnant saltwater to enhance corrosion of AZ31B (marked in red circles in Figure 10). The galvanic effect must have played a role in this enhanced corrosion of AZ31B alloy, which should be further investigated using electrochemical measurement. As seen in Figure 10, the steel rivet head, which was directly exposed to salt fog, also exhibited greater corrosion with increasing exposure time.

Tensile shear testing was conducted for post-corroded lap shear coupons with different exposure times (24 h, 100 h, and 200 h). Figure 11 plots examples of load and displacement curves for the first set of F-SPR joints with different corrosion exposure times. New, pristine F-SPR joints (set#1) made prior to corrosion testing had an average lap shear failure load of 5.07 ± 0.11 kN, which is similar to the tensile shear failure load results from the previous testing (5.18 kN). The retained tensile peak failure loads were 4.23 kN, 4.48 kN, and 4.81 kN for 24 h, 100 h, and 200 h of salt

spray exposure to F-SPR joints, respectively. The test results were somewhat scattered, potentially because of stagnated corrosion products on the step, as shown in Figure 5(b). These stagnated corrosion products could prevent the infiltration of NaCl solution into the joint area and delay corrosion at the joint. Another possible reason for the scattered results may be non-uniform corrosion exposure from different sample loading locations in the corrosion chamber. This corrosion testing was an initial trial to assess the corrosion behavior of F-SPR joints. For this reason, two additional testing sets (#2 and #3) were performed for statistical study. Figure 12 summarizes the average loss in joint strength (%) as result of corrosion testing. Percentage (%) of retained failure load was normalized by the original peak load of non-corroded samples for individual sets. As can be seen, joint integrity was gradually decreased with increased corrosion exposure time, as expected. The average retained strength of the corroded F-SPR joint was 81.2% of the original F-SPR joint strength at 200 hour exposure time.

Figure 13 shows the fractography of lap shear tensile-tested post-corroded F-SPR joints from each set. It can be seen that white products (indicated by red arrow) at the joint area is corrosion product of $MgO/Mg(OH)_2$. As can be seen, corrosion of AZ31 at the joint area is not uniform, which leads to some scatter in retained joint strength. All F-SPR joints show the same failure mode, where the rivet pulled out of the AZ31B sheet. This failure mode is the same as that for the pristine F-SPR joints seen in Figure 7(a).

Cross-sectional and backside views of post-corroded F-SPR specimens with 24 h, 100 h, and 200 h exposure times are shown in Figure 14. Pitting corrosion on AZ31B was observed for all exposure times (red arrow in Figure 14). Also, the backside view of the F-SPR joint showed the progression of corrosion on the edges of AZ31B, as well as white corrosion products consistent with $MgO/Mg(OH)_2$ accumulating at the joint area. Figure 15 shows EDS mapping at the F-SPR

joint interface at a corrosion exposure time of 24 h, as shown in Figure 14(a). Figure 15(a–e) depict acquired elements of carbon, iron, magnesium, and oxygen on the left side of the joint interface. Some carbon fibers were plunged into the joint interface between the steel rivet and the AZ31B because of riveting with a downward axial force. Then, some flash of AZ31B was partially imbedded into the CFRP as a result of the plunge. No major corrosion of the steel rivet was observed at the joint interface, but some corrosion at the steel rivet head was seen. This is likely due to the sacrificial anode effect from the large potential difference between the steel rivet and AZ31B, as stated previously. That is, AZ31B is preferentially corroded before the steel rivet. A similar example is zinc-coated steel where the zinc coating layer is protecting the steel substrate from the corrosion medium as a sacrificial anode. As a result, corrosion of AZ31B near the steel interface, Figure 15(d–e). Figure 15(f–j), shows a similar result on the right side of the joint interface.

Figure 16 illustrates potential corrosion mechanisms of the F-SPR joint from a cross-sectional view. First, the mechanism is general corrosion of an individual material (e.g., AZ31B, steel rivet, and CFRP) in which it is directly exposed to the corrosion medium. As already shown in Figures 10 and 13, significant corrosion of the steel rivet head and AZ31B sheet was observed with increased corrosion exposure time. Detailed corrosion mechanisms of carbon steel [28] and Mg alloys [36] can be found elsewhere. No significant corrosion of the CFRP was observed. For the crevice corrosion at the gap between the CFRP and AZ31B, the corrosion medium or solution can stagnate in the confined gap or local area, leading to local chemistry different from the free solution in the surrounding environment. This could be one of the causes that AZ31B formed pitting inside the gap without significant general corrosion, as observed in Figure 14. This crevice corrosion can be mitigated by applying an adhesive or sealant at the joint interface to prevent infiltration of the

corrosion medium [25,26]. Finally, the last mechanism is galvanic corrosion, in which two dissimilar materials are in electrical contact under the presence of an electrolyte [37]. As seen in Figures 14 and 15, the steel rivet is in contact with carbon fibers in the epoxy resin as well as the AZ31B sheet. Therefore, two galvanic couples can be formed: carbon fibers paired with the steel rivet and AZ31B paired with the steel rivet. From corrosion potential measurements, a Mg alloy such as AZ31B is the most active metal in the galvanic series [24]. Therefore, Mg alloys can act as active anodes when they are in physical contact with other materials [38]. Because of the sacrificial anode effect (i.e., AZ31B corrodes first rather than the steel rivet), no significant corrosion of the steel rivet at the joint interface was observed, which may be a reason why joint integrity is still maintained after up to 200 h of corrosion testing.

4. Conclusions

Thermoset CFRP and Mg alloy AZ31B were spot joined by F-SPR. An average lap shear tensile load of 5.18 kN was achieved with pull-out of AZ31B as the failure mode, indicating good mechanical interlocking between the steel rivet and the AZ31B. Similarly, an average cross-tension load of 2.81 kN was achieved with significant bending of AZ31B prior to final failure. Based on corrosion potential measurements, AZ31B was the most active material while thermoset CFRP was the most noble material for the galvanic corrosion series. The steel rivet was between the CFRP and the AZ31B. ASTM B-117 salt fog corrosion testing revealed extensive corrosion of AZ31B at the joint area. Post-corroded F-SPR joint integrity retained 81.2% of the original F-SPR joint strength with AZ31B pull-out failure mode at 200 hour exposure time.

Acknowledgements

This research was financially sponsored by the U.S. Department Energy Vehicle Technology Offices, as part of the Joining Core Program. Oak Ridge National Laboratory (ORNL) is managed by UT-Battelle, LLC for the U.S. Department of Energy under Contract DE-AC05-00OR22725.

Reference

[1] Dilthey U, and Stein L., 2006, "Multimaterial car body design: challenge for welding and joining," Sci. Technol. Weld. Joi., **11**, pp.135–141.

[2] Meschut, G., Janzen, V., Olfermann T., 2014, "Innovative and highly productive joining technologies for multi-material lightweight car body structures," J. Mater. Eng. Perf., **23**, pp.1515–1523.

[3] Skszek, T., Zaluzec, M., Conklin, J., Wager, D., 2015, "MMLV: Project overview," SAE Technical Paper. 2015-01-0407 (doi:10.4271/2015-01-0407).

[4] Kleinbaum, S., Jiang, C., Logan, S., 2019, "Enabling sustainable transportation through joining of dissimilar lightweight materials," MRS Bull. **44**, pp.608-612.

[5] Luo, A.A., and Sachdev, A.K., 2012, Advances in Wrought Magnesium Alloys: Fundamentals of Processing, Properties and Applications, Woodhead Publishing, Cambridge, UK.

[6] Adam, H., 1997, "Carbon fibre in automotive applications," Mater. Des. **18**, pp.349–355.

[7] Edwards, K.L., 1998, "An overview of the technology of fibre-reinforced plastics for design purpose," Mater. Des., **19**, pp.1–10.

[8] Zhang, Z., Shan, J., Tan, X., Zhang, J., 2017, "Improvement of the laser joining of CFRP and aluminum via laser pre-treatment," Int. J. Adv. Manuf. Technol., **90**, pp.3465-3472.

[9] Nagatsuka, K., Xiao, B., Wu, L., Nakata, K., Saeki, S., Kitamoto, Y., Iwamoto, Y., 2018, "Resistance spot welding of metal/carbon-fibre-reinforced plastics and applying silane coupling treatment," Sci. Technol. Weld. Join., **23**, pp.181-186.

[10] Goushegir, S.M., dos Santos, J.F., Amancio-Filho S.T., 2014, "Friction spot joining of aluminum AA2024/carbon-fiber reinforced poly(phenylene sulfide) composite single lap joints: Microstructure and mechanical performance," Mater. Des., **54**, pp.196-206.

[11] Esteves, J.V., Goushegir, S.M., dos Santos, J.F., Canto, L.B., Hage, Jr E., Amancio-Filho, S.T., 2015, "Friction spot joining of aluminum AA6181-T4 and carbon fiber-reinforced poly(phenylene sulfide): Effects of process parameters on the microstructure and mechanical strength," Mater. Des., **66**, pp.437-445.

[12] Nagatsuka, K., Yoshida, S., Tsuchiya, A., Nakata, K., 2015, "Direct joining of carbon-fiber-reinforced plastic to an aluminum alloy using friction lap joining," Composites B., **73**, pp.82-88.

[13] Balle, F., Wagner, G., Eifler, D., 2009, "Ultrasonic metal welding of aluminium sheets to carbon fibre reinforced thermoplastic composites," Adv. Eng. Mater., **11**, pp.35-39.

[14] Min, J., Li, Y., Li, J., Carlson, B.E., Lin, J., 2015, "Friction stir blind riveting of carbon fiber-reinforced polymer composite and aluminum alloy sheets," Int. J. Adv. Manuf. Technol., **76**, pp.1403-1410.

[15] Lim, Y.C., Park, H., Jang, J., McMurray, J.W., Lokitz, B.S., Keum, J.K., Wu, Z., Feng, Z., 2018, "Dissimilar materials joining of carbon fiber polymer to dual phase 980 by friction bit joining, adhesive bonding, and weldbonding," Metals. 8, pp.865.

[16] Amancio-Filho, S.T., Bueno, C., dos Santos, J.F., Huber, N., Hage, Jr E., 2011, "On the feasibility of friction spot joining in magnesium/fiber-reinforced polymer composite hybrid structures," Mater. Sci. Eng. A., **528**, pp.3841-3848.

[17] Arkhurst, B.M., Kim, J.H., Lee, M-Y., 2019, "Hot metal pressing joining of carbon fiber reinforced plastics to AZ31 Mg alloy and the effect of the oxide surface layer on joint strength," Appl. Surf. Sci., **477**, pp.241-256.

[18] Doege, E., and Droder, K., 2001, "Sheet Metal Forming of Magnesium Wrought Alloys—Formability and Process Technology," J. Mater. Process. Technol., **115**, pp.14–19.

[19] Hahn, O., and Horstmann, M., 2007, "Mechanical joining of magnesium components by means of inductive heating—realization and capability," Mater. Sci. Forum, **539/543**, pp.1638–1643.

[20] Durandet, Y., Deam, R., Beer, A., Song, W., Blacket, S., 2010, "Laser assisted self-pierce riveting of AZ31 magnesium alloy strips," Mater. Des., **31**, pp.S13–S16.

[21] Wang, J.W., Liu, Z.X., Shang, Y., Liu, A.L., Wang, M. X., Sun, R.N., Wang, P-C., 2011, "Self-piercing riveting of wrought magnesium AZ31 Sheets," ASME J. Manuf. Sci. Eng., **133**, pp.031009.

[22] Li ,Y.B., Wei, Z.Y., Wang, Z.Z., Li, Y.T., 2013, "Friction self-piercing riveting of aluminum alloy AA6061-T6 to magnesium alloy AZ31B," J. Manuf. Sci. Eng., **134**, pp.061007.

[23] Liu, X., Lim, Y.C., Li, Y.B., Tang, W., Ma, Y., Feng, Z., Ni, J., 2016, "Effects of process parameters on friction self-piercing riveting of dissimilar materials," J. Mater. Proc. Technol., **237**, pp.19-30.

[24] LeBozec, N., LeGac, A., Thierry, D., 2012, "Corrosion performance and mechanical properties of joined automotive materials," Mater. Corros., **63**, pp.408-415.

[25] Lim, Y.C., Squires, L., Pan, T-Y., Miles, M., Song, G-L., Wang, Y., Feng, Z., 2015. "Study of mechanical joint strength of aluminum alloy 7075-T6 and dual phase steel 980 welded by friction bit joining and weld-bonding under corrosion medium," Mater. Des., **69**, pp.37-43.

[26] Lim, Y.C., Squires, L., Pan, T-Y., Miles, M., Keum, J.K., Song, G-L., Wang, Y., Feng, Z., 2017, "Corrosion behaviour of friction-bit-joined and weld-bonded AA7075-T6/galvannealed DP980," Sci. Technol. Weld. Join., **22**, pp.455-464.

[27] Nassar, S.A., and Sakai, K., 2015, "Effect of cyclic heat, humidity and joining method on the static and dynamic performance of lightweight multimaterial single-lap joints," J. Manuf. Sci. Eng., **137**, pp.051026-1-11.

[28] ASTM G82-98, Standard guide for development and use of a galvanic series for predicting galvanic corrosion performance, ASTM 3.02, **1998**, pp. 356–361

[29] Li, D., Chrysanthou, A., Patel, I., Williams, G., 2017, "Self-piercing riveting-a review," Int. J. Adv. Manu. Technol., **92**, pp.1777-1824.

[30] Han, L., Thornton, M., Li, D., 2010, "Effect of setting velocity on self-piercing riveting process and joint behaviour for automotive applications," SAE Technical Paper, pp.01-0966.

[31] Fajardo, S., and Frankel, G.S., 2015, "Effect of impurities on the enhanced catalytic activity for hydrogen evolution in high purity magnesium," Electrochim. Acta, **165**, pp. 255–267.

[32] Singh, I.B., Singh, M., Das, S., 2015, "A comparative corrosion behavior of Mg, AZ31 and AZ91 alloys in 3.5% NaCl solution," J. Magnes. Alloy, **3**, pp.142-148.

[33] Tefashe, U.M., Dauphin-Ducharme, P., Danaie, M., Cano, Z.P., Kish, J.R., Botton, G.A., Mauzerolla, J., 2015, "Localized corrosion behavior of AZ31B magnesium alloy with an electrodeposited poly(3,4-ethylenedioxythiophene) coating," J. Electrochem. Soc., **162**, pp.C536-C544.

[34] Osorio, W.R., Peixoto, L.C., Garcia, L.R., Garcia, A., 2009, "Electrochemcial corrosion response of a low carbon heat treated steel in a NaCl solution," Mater. Corro., **60**, pp.804-812.

[35] Pan, Y., Wu, G., Cheng, X., Zhang, Z., Li, M., Ji, S., Huang, Z., 2015, "Galvanic corrosion behaviour of carbon fibre reinforced polymer/magnesium alloys coupling," Corro. Sci., **98**, pp.672-677.

[36] Ghali, E., Dietzel, W., Kainer, K-U., 2004, "General and localized corrosion of magnesium alloys: a critical review," J. Mater. Eng. Perf., **13**, pp.7-23.

[37] Revie RW., 2011, Uhlig's corrosion handbook. 3rd ed. Hoboken: John Wiley & Sons, Inc.

[38] Song, G., Johannesson, B., Hapugoda, S., StJohn, D., 2004, "Galvanic corrosion of magnesium alloy AZ91D in contact with an aluminum alloy, steel and zinc," Corro. Sci., **46**, pp.955-977.

List of Table Caption

Table 1. Analyzed chemical compositions (% wt) of AZ31B and the steel rivet by inductively coupled plasma and combustion techniques.

Table 2. Mechanical properties of thermoset CFRP (G-83 prepreg), AZ31B, and steel rivet at room temperature.

Table 3. Summary of F-SPR conditions.

Table 4. Summary of lap shear tensile and cross-tension testing.

Table 5. Corrosion potential of each material at the end of measurement.

List of Figure Caption

FIGURE 1. Schematic of rivet and die geometry with dimensions (mm).

FIGURE 2. Schematic of lap shear and cross-tension coupons with dimension (mm).

FIGURE 3. Schematic of F-SPR [22,23].

FIGURE 4. Schematic of corrosion potential measurement for AZ31B, thermoset CFRP, steel rivet, or graphite as a working electrode.

FIGURE 5. (a) Pristine F-SPR specimens (set#1) prior to corrosion testing. (b) Mounted F-SPR joints on Teflon rack in the corrosion chamber for ASTM B-117 testing.

FIGURE 6. Summary of load and displacement curves from (a) lap shear tensile testing and (b) cross-tension testing.

FIGURE 7. Fractographic images from mechanical testing of F-SPR joints: (a) lap shear coupon, (b) cross-tension coupon, and (c) side view of AZ31B from cross-tension coupon.

FIGURE 8. Cross-sectional view of F-SPR joint. (a) Optical image, (b) magnified SEM image at interface between rivet head and CFRP, (c) magnified SEM image at joint interface between rivet and AZ31B.

FIGURE 9. Corrosion potential (E_{corr}) of AZ31B, steel rivet, CFRP, and graphite rod with increasing time in 0.1 M NaCl at room temperature.

FIGURE 10. Optical images of post-corroded F-SPR joints (set#1) with different exposure times: (a) 24 h, (b) 100 h, and (c) 200 h. Corrosion ditches on the AZ31B are marked in red circles.

FIGURE 11. Load versus displacement curves from lap shear tensile testing for corrosion-exposed F-SPR joints.

FIGURE 12. Summary of the retained original lap shear load (%) from three sets of ASTM B-117 testing.

Journal of Manufacturing Science and Engineering. Received May 18, 2020;
Accepted manuscript posted May 20, 2020. doi:10.1115/1.4048378

FIGURE 13. Fractography of lap shear tensile-tested F-SPR joints from each three set testing with different corrosion exposure times.

FIGURE 14. Cross-sectional and backside view of post-corroded F-SPR joints. (a) and (d): 24 h, (b) and (e): 100 h, (c) and (f): 200 h.

FIGURE 15. EDS mapping at F-SPR joint interface: left side joint interface (a–e); right side joint interface (f–j).

FIGURE 16. Schematic of F-SPR joint with potential corrosion mechanisms, including general, crevice and galvanic corrosion.

Journal of Manufacturing Science and Engineering. Received May 18, 2020;
Accepted manuscript posted May 20, 2020. doi:10.1115/1.4048378

Table 1. Analyzed chemical compositions (% wt) of AZ31B and the steel rivet by inductively coupled plasma and combustion techniques.

Element	AZ31B	Steel rivet
C	–	0.18
Al	2.99	0.05
Zn	0.91	<0.01
Mn	0.31	0.74
Mo	–	<0.01
Cr	–	0.02
Ca	<0.005	–
Cu	<10 ppm	0.01
Fe	21 ppm	Balance
Nb	–	<0.01
Ni	<10 ppm	0.01
Si	<0.005	0.04
Sn	–	<0.01
Re	<0.005	–
Y	<0.005	–
Zr	0.018	–
P	–	0.012
S	–	0.002
Mg	Balance	–
Others	<0.01	–

Journal of Manufacturing Science and Engineering. Received May 18, 2020;
Accepted manuscript posted May 20, 2020. doi:10.1115/1.4048378

Table 2. Mechanical properties of thermoset CFRP (G-83 prepreg), AZ31B, and steel rivet at room temperature.

Material	Tensile strength (MPa)	Elongation (%)
CFRP (G-83 prepreg)	827	–
AZ31B	285	16.1
Steel rivet	463	26.4

Journal of Manufacturing Science and Engineering. Received May 18, 2020;
Accepted manuscript posted May 20, 2020. doi:10.1115/1.4048378

Table 3. Summary of F-SPR conditions.

Spindle rotational speed (rpm)	1500
Downward plunge depth (mm)	6.12
Downward plunge speed (mm/s)	2.86

Journal of Manufacturing Science and Engineering. Received May 18, 2020;
Accepted manuscript posted May 20, 2020. doi:10.1115/1.4048378

Table 4. Summary of lap shear tensile and cross-tension testing.

	Lap shear tensile testing		Cross-tension testing	
Sample #	Peak failure load (kN)	Absorbed energy (J)	Peak failure load (kN)	Absorbed energy (J)
1	5.12	26.44	2.80	15.70
2	5.27	27.03	2.92	20.02
3	5.3	26.39	2.71	18.02
4	5.04	24.33	-	-
Average±STD	5.18±0.12	26.05±1.18	2.81±0.11	17.91±2.16

Journal of Manufacturing Science and Engineering. Received May 18, 2020;
Accepted manuscript posted May 20, 2020. doi:10.1115/1.4048378

Table 5. Corrosion potential of each material at the end of measurement.

Material	Graphite rod	Thermoset CFRP	Steel rivet	AZ31B
E_{corr}	0.24 V_{SCE}	0.23V_{SCE}	−0.6V_{SCE}	−1.55V_{SCE}

Journal of Manufacturing Science and Engineering. Received May 18, 2020;
Accepted manuscript posted May 20, 2020. doi:10.1115/1.4048378

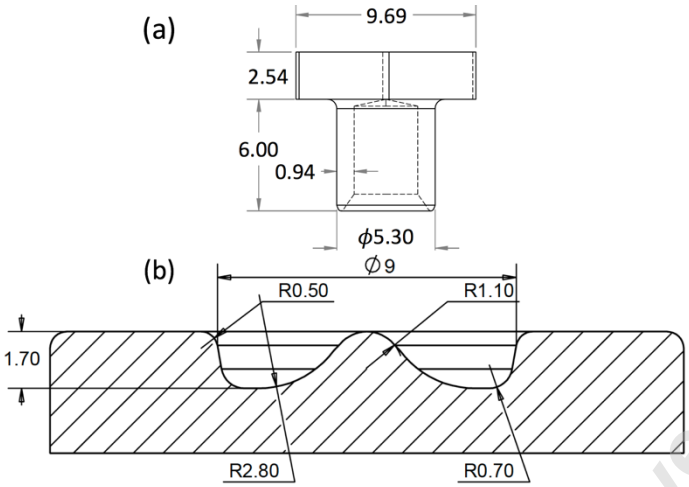

FIGURE 1. Schematic of rivet and die geometry with dimensions (mm).

Journal of Manufacturing Science and Engineering. Received May 18, 2020;
Accepted manuscript posted May 20, 2020. doi:10.1115/1.4048378

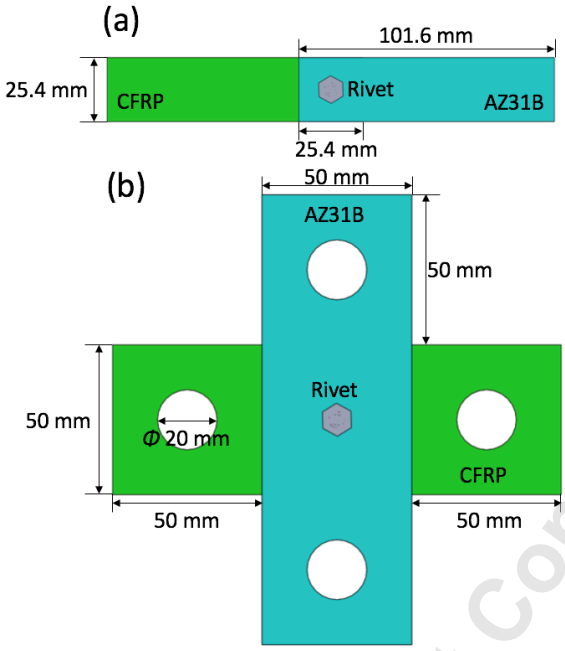

FIGURE 2. Schematic of lap shear and cross-tension coupons with dimension (mm).

Journal of Manufacturing Science and Engineering. Received May 18, 2020;
Accepted manuscript posted May 20, 2020. doi:10.1115/1.4048378

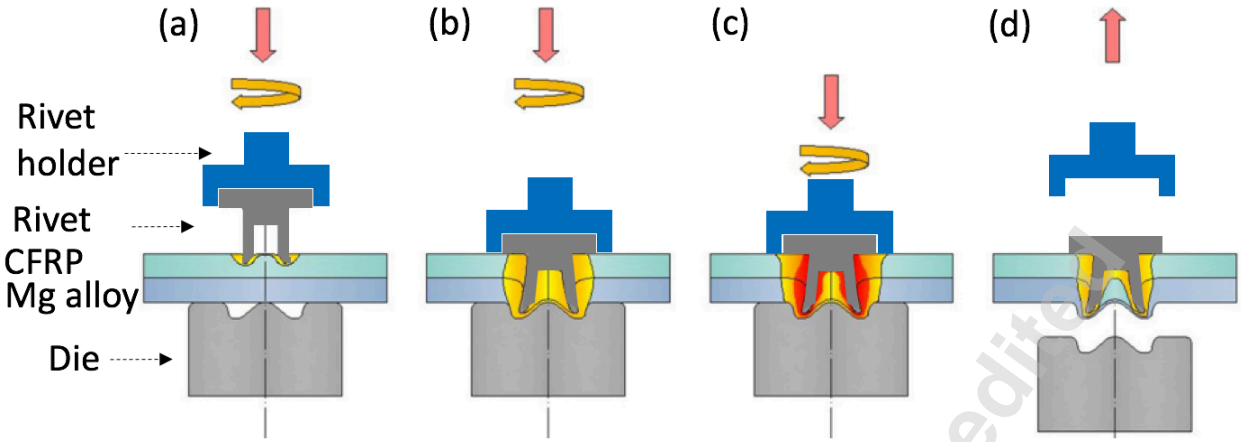

FIGURE 3. Schematic of F-SPR [22,23].

Journal of Manufacturing Science and Engineering. Received May 18, 2020;
Accepted manuscript posted May 20, 2020. doi:10.1115/1.4048378

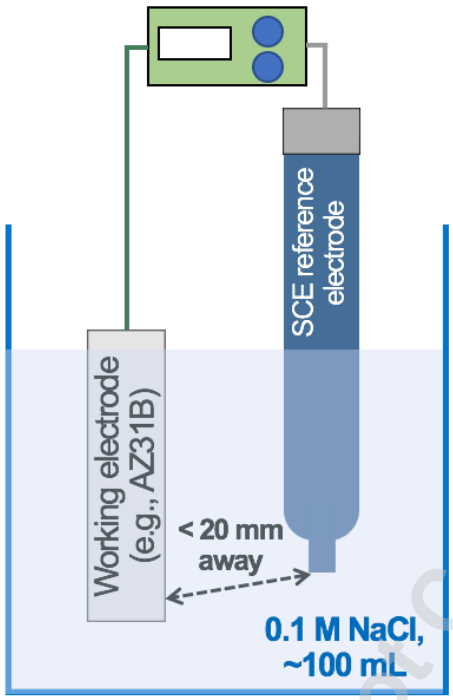

FIGURE 4. Schematic of corrosion potential measurement for AZ31B, thermoset CFRP, steel rivet, or graphite as a working electrode.

Journal of Manufacturing Science and Engineering. Received May 18, 2020;
Accepted manuscript posted May 20, 2020. doi:10.1115/1.4048378

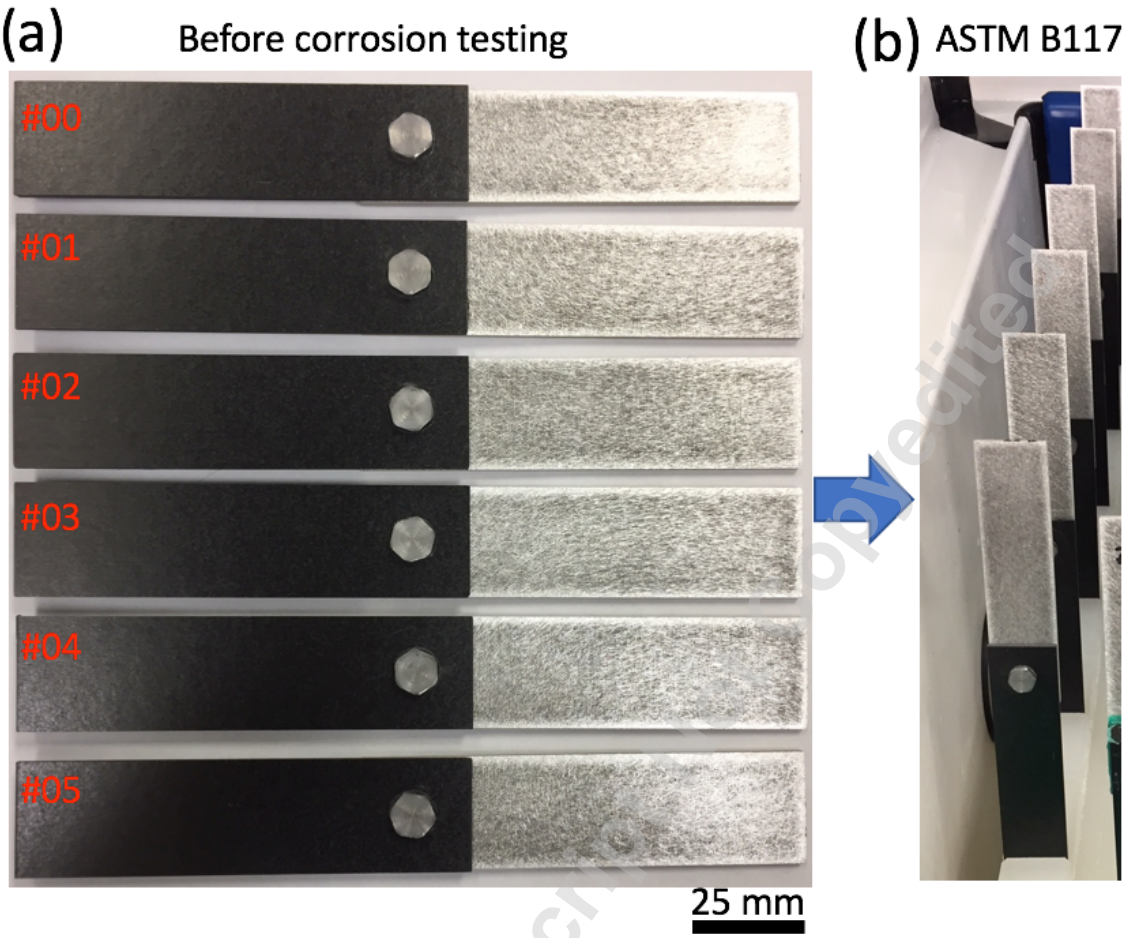

FIGURE 5. (a) Pristine F-SPR specimens (set#1) prior to corrosion testing. (b) Mounted F-SPR joints on Teflon rack in the corrosion chamber for ASTM B-117 testing.

Journal of Manufacturing Science and Engineering. Received May 18, 2020;
Accepted manuscript posted May 20, 2020. doi:10.1115/1.4048378

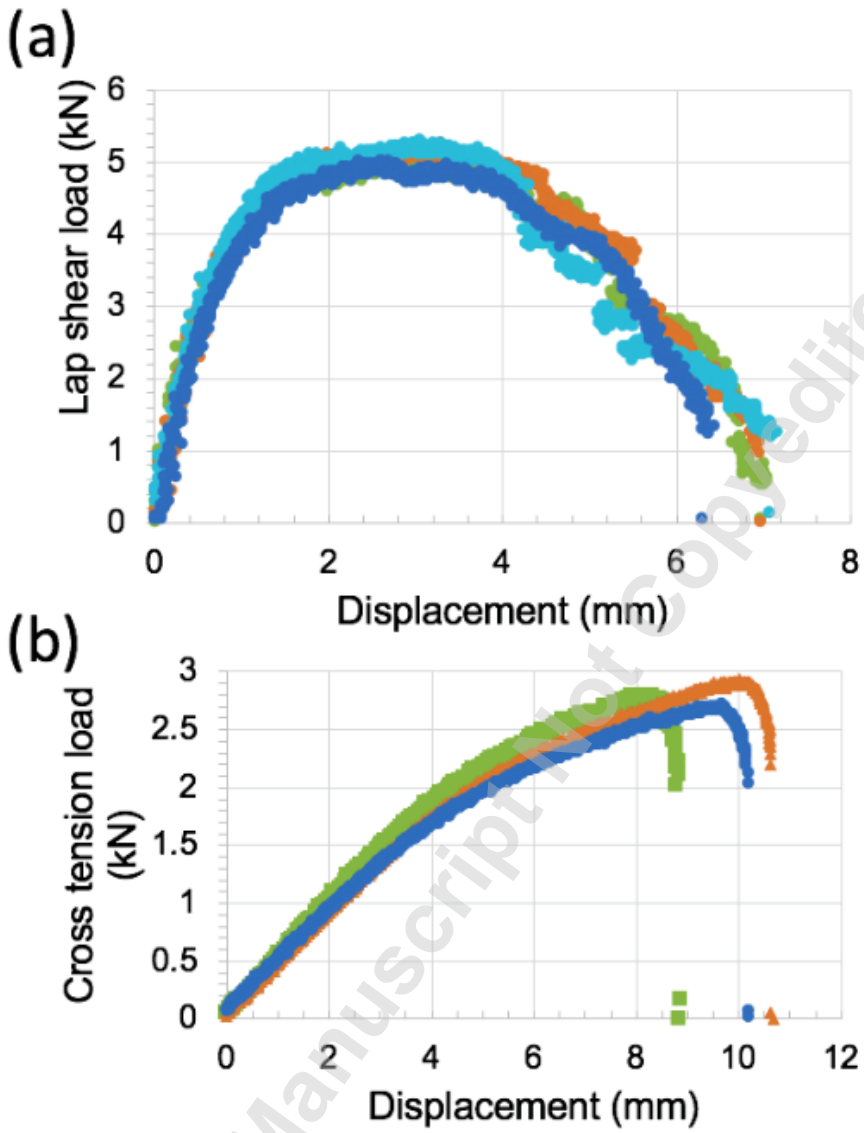

FIGURE 6. Summary of load and displacement curves from (a) lap shear tensile testing and (b) cross-tension testing.

Journal of Manufacturing Science and Engineering. Received May 18, 2020;
Accepted manuscript posted May 20, 2020. doi:10.1115/1.4048378

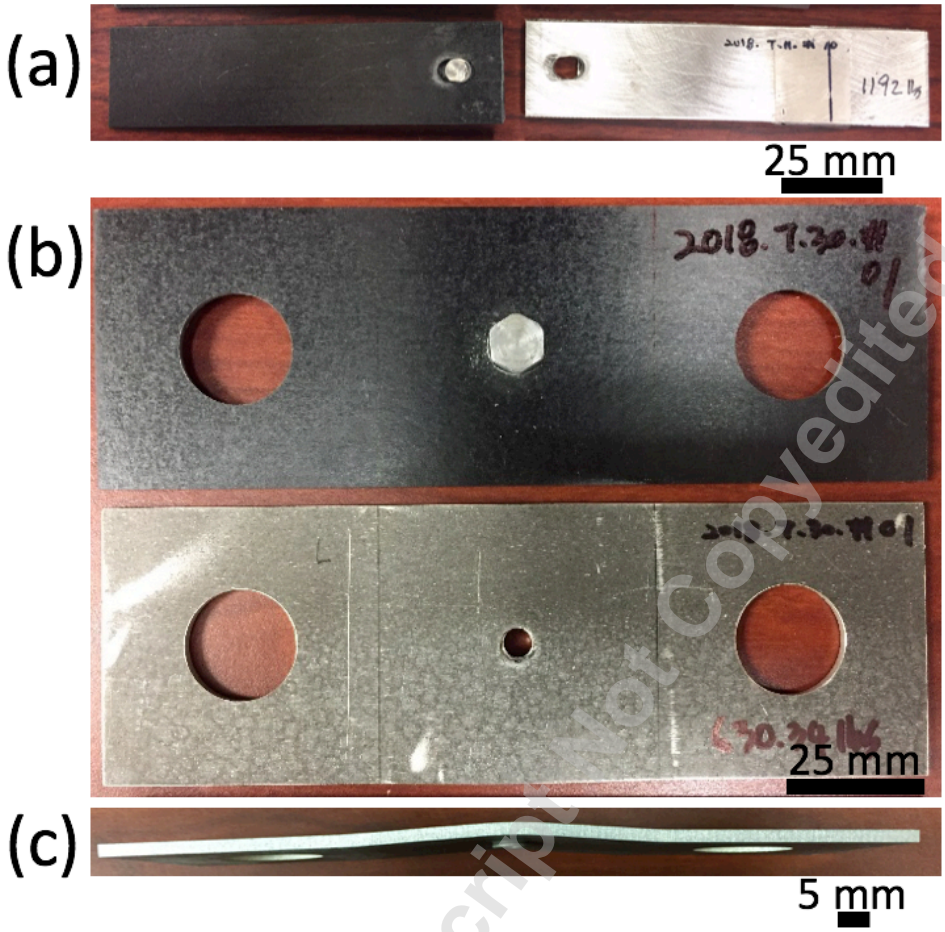

FIGURE 7. Fractographic images from mechanical testing of F-SPR joints: (a) lap shear coupon, (b) cross-tension coupon, and (c) side view of AZ31B from cross-tension coupon.

Journal of Manufacturing Science and Engineering. Received May 18, 2020;
Accepted manuscript posted May 20, 2020. doi:10.1115/1.4048378

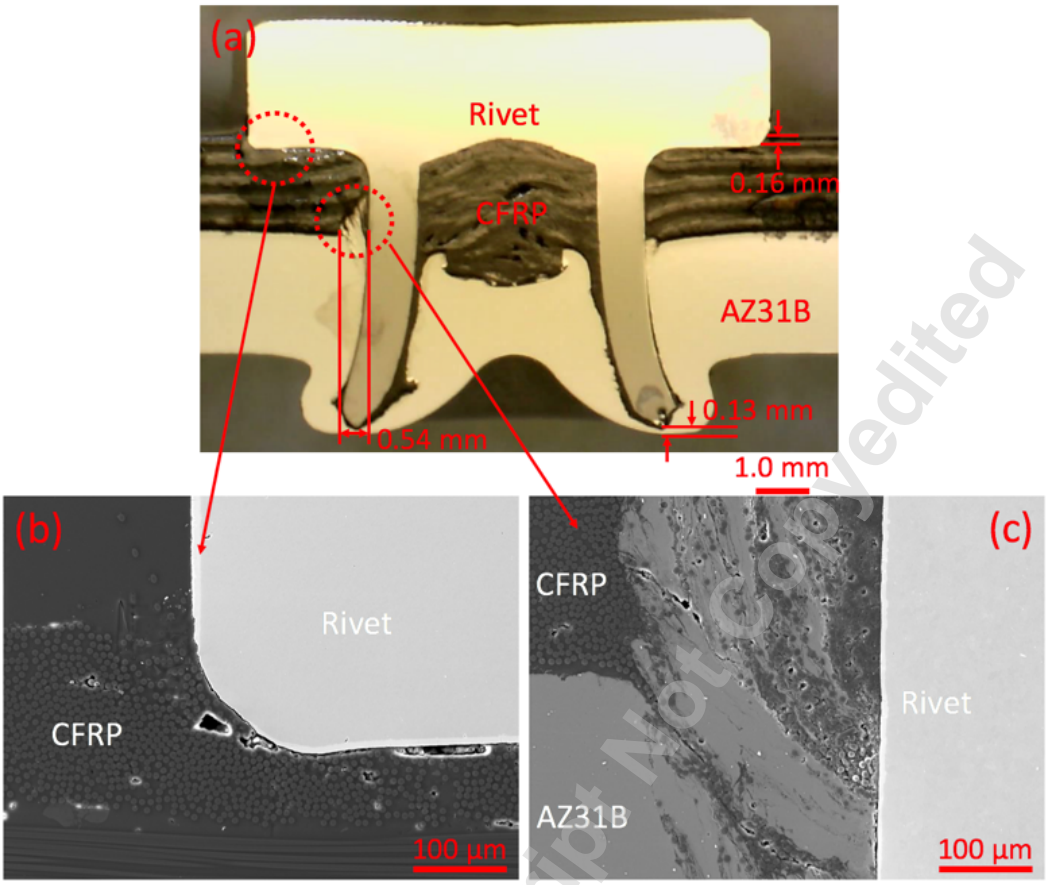

FIGURE 8. Cross-sectional view of F-SPR joint. (a) Optical image, (b) magnified SEM image at interface between rivet head and CFRP, (c) magnified SEM image at joint interface between rivet and AZ31B.

Journal of Manufacturing Science and Engineering. Received May 18, 2020;
Accepted manuscript posted May 20, 2020. doi:10.1115/1.4048378

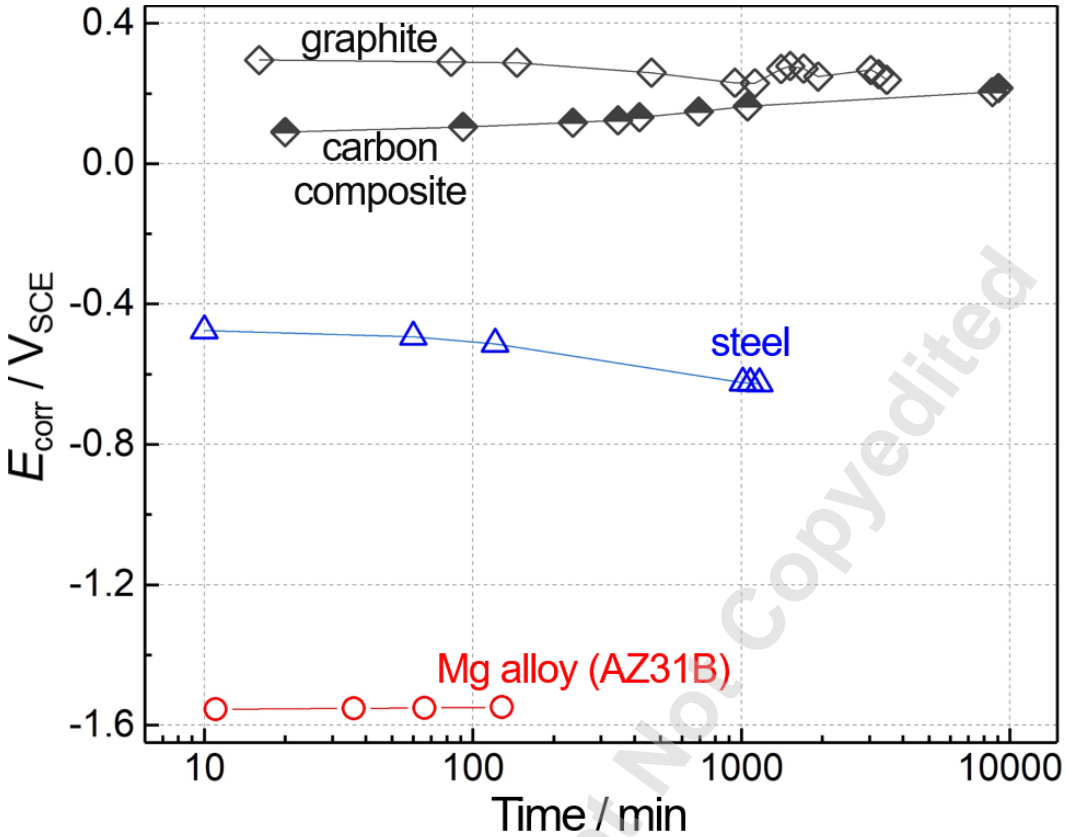

FIGURE 9. Corrosion potential (E_{corr}) of AZ31B, steel rivet, CFRP, and graphite rod with increasing time in 0.1 M NaCl at room temperature.

Journal of Manufacturing Science and Engineering. Received May 18, 2020;
Accepted manuscript posted May 20, 2020. doi:10.1115/1.4048378

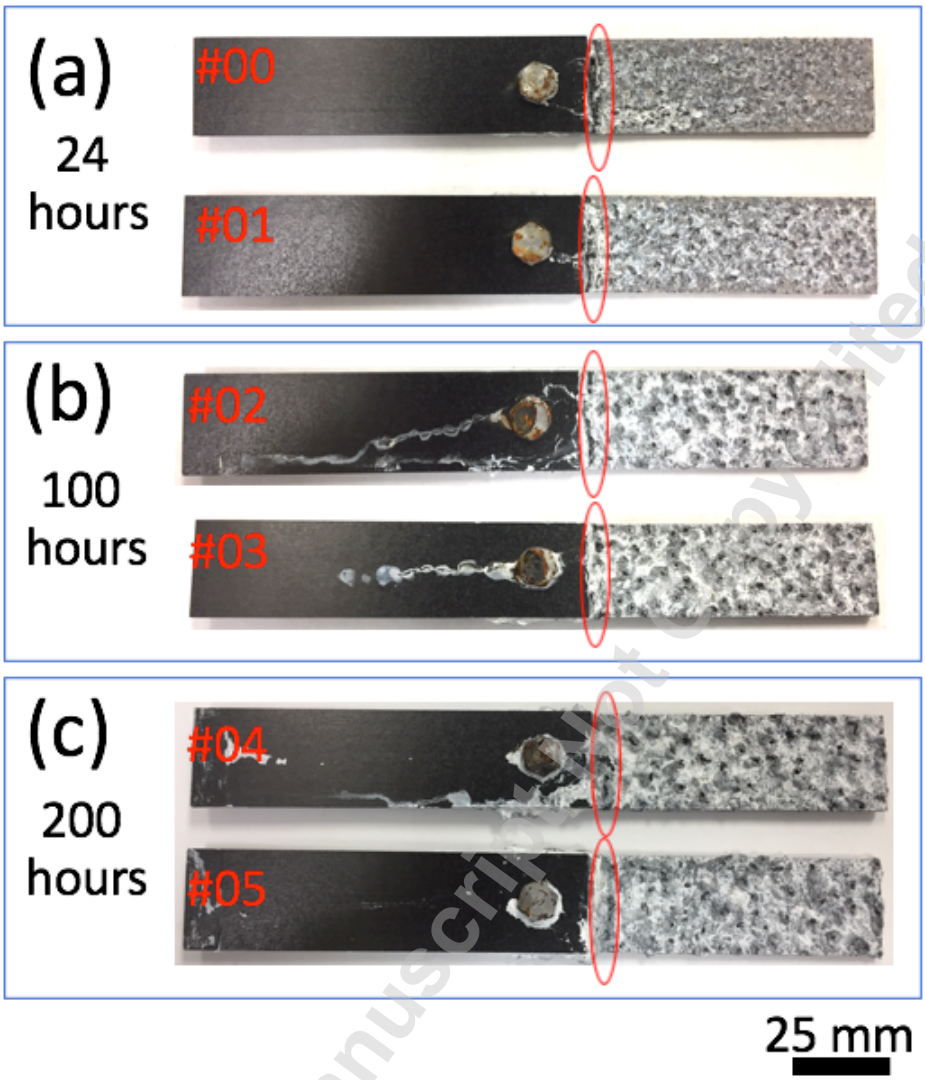

FIGURE 10. Optical images of post-corroded F-SPR joints (set#1) with different exposure times: (a) 24 h, (b) 100 h, and (c) 200 h. Corrosion ditches on the AZ31B are marked in red circles.

Journal of Manufacturing Science and Engineering. Received May 18, 2020;
Accepted manuscript posted May 20, 2020. doi:10.1115/1.4048378

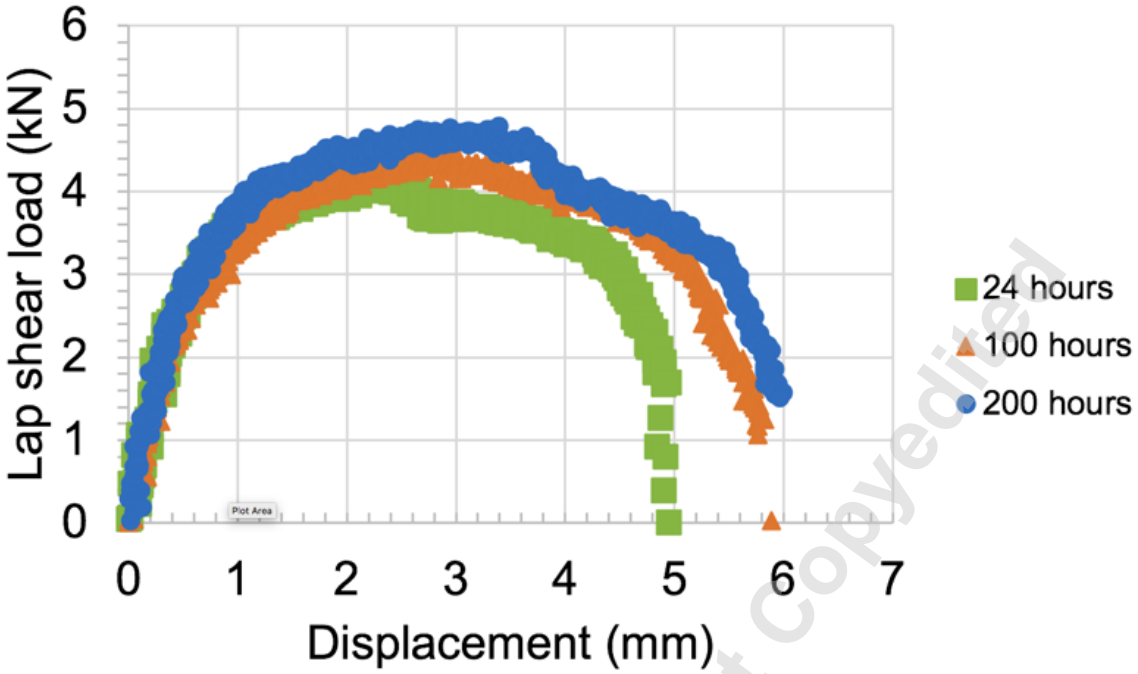

FIGURE 11. Load versus displacement curves from lap shear tensile testing for corrosion-exposed F-SPR joints.

Journal of Manufacturing Science and Engineering. Received May 18, 2020;
Accepted manuscript posted May 20, 2020. doi:10.1115/1.4048378

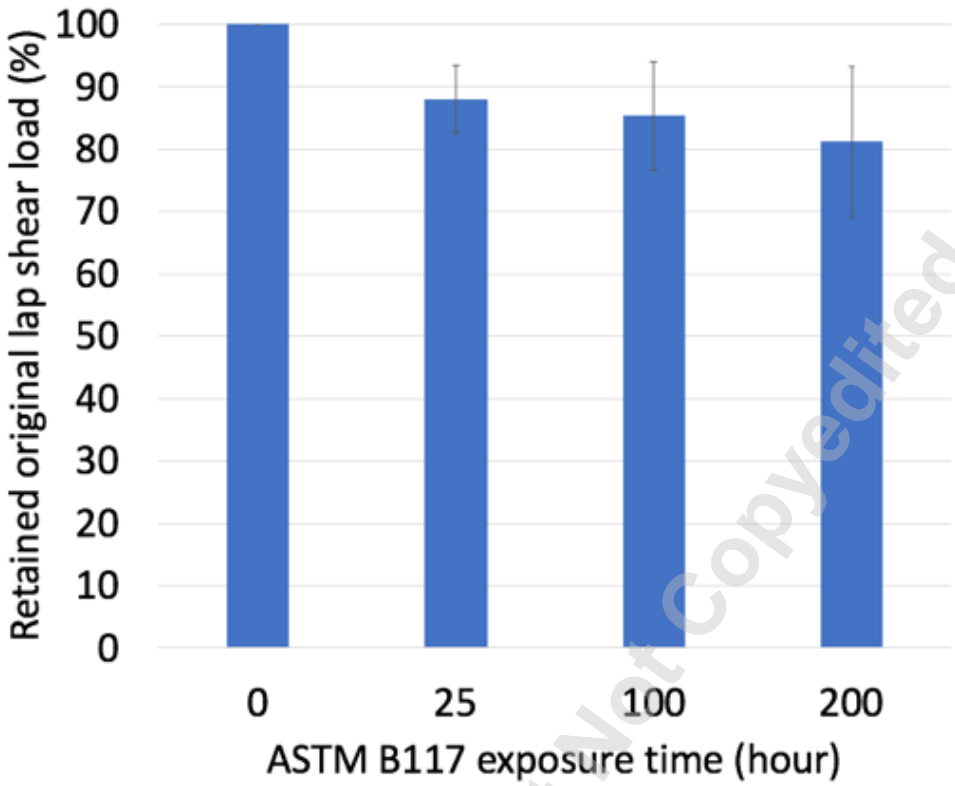

FIGURE 12. Summary of the retained original lap shear load (%) from three sets of ASTM B-117 testing.

Journal of Manufacturing Science and Engineering. Received May 18, 2020;
Accepted manuscript posted May 20, 2020. doi:10.1115/1.4048378

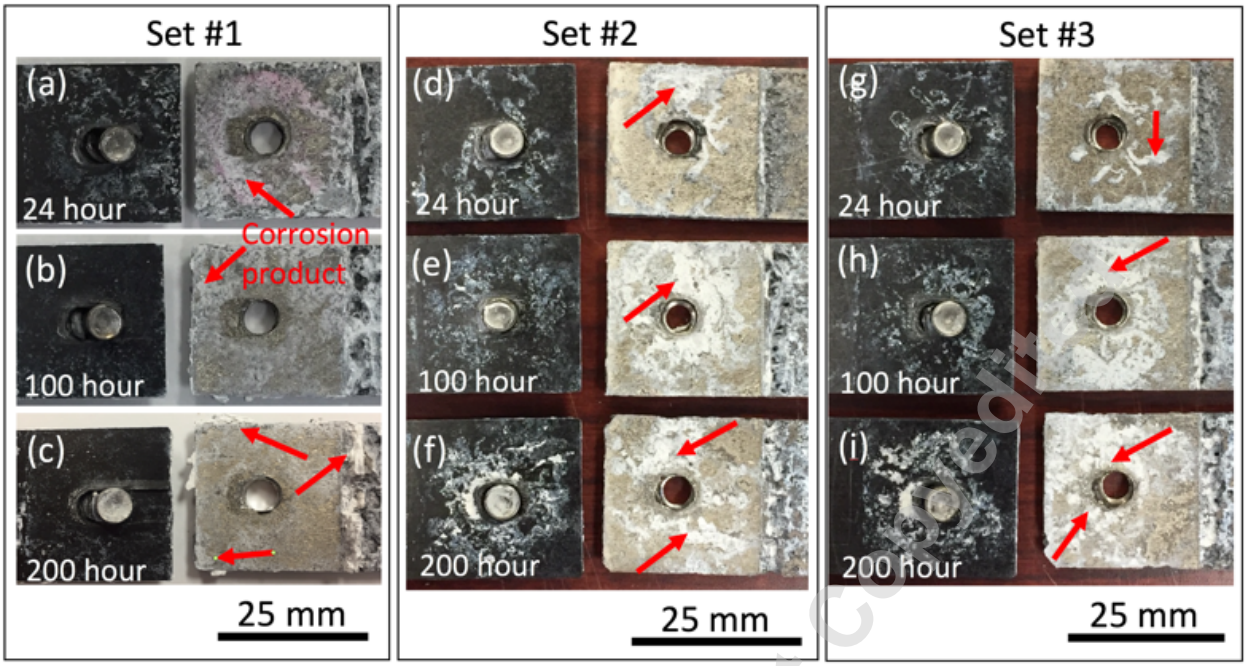

FIGURE 13. Fractography of lap shear tensile-tested F-SPR joints from each three set testing with different corrosion exposure times.

Journal of Manufacturing Science and Engineering. Received May 18, 2020;
Accepted manuscript posted May 20, 2020. doi:10.1115/1.4048378

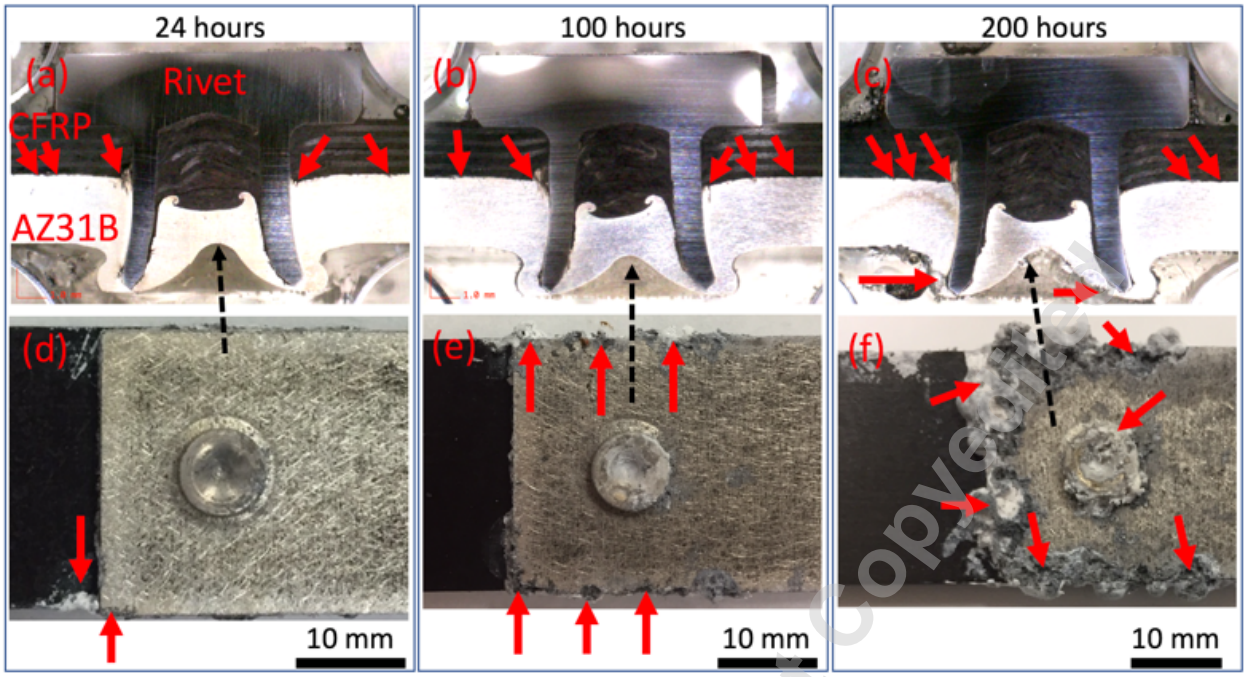

FIGURE 14. Cross-sectional and backside view of post-corroded F-SPR joints. (a) and (d): 24 h, (b) and (e): 100 h, (c) and (f): 200 h.

Journal of Manufacturing Science and Engineering. Received May 18, 2020;
Accepted manuscript posted May 20, 2020. doi:10.1115/1.4048378

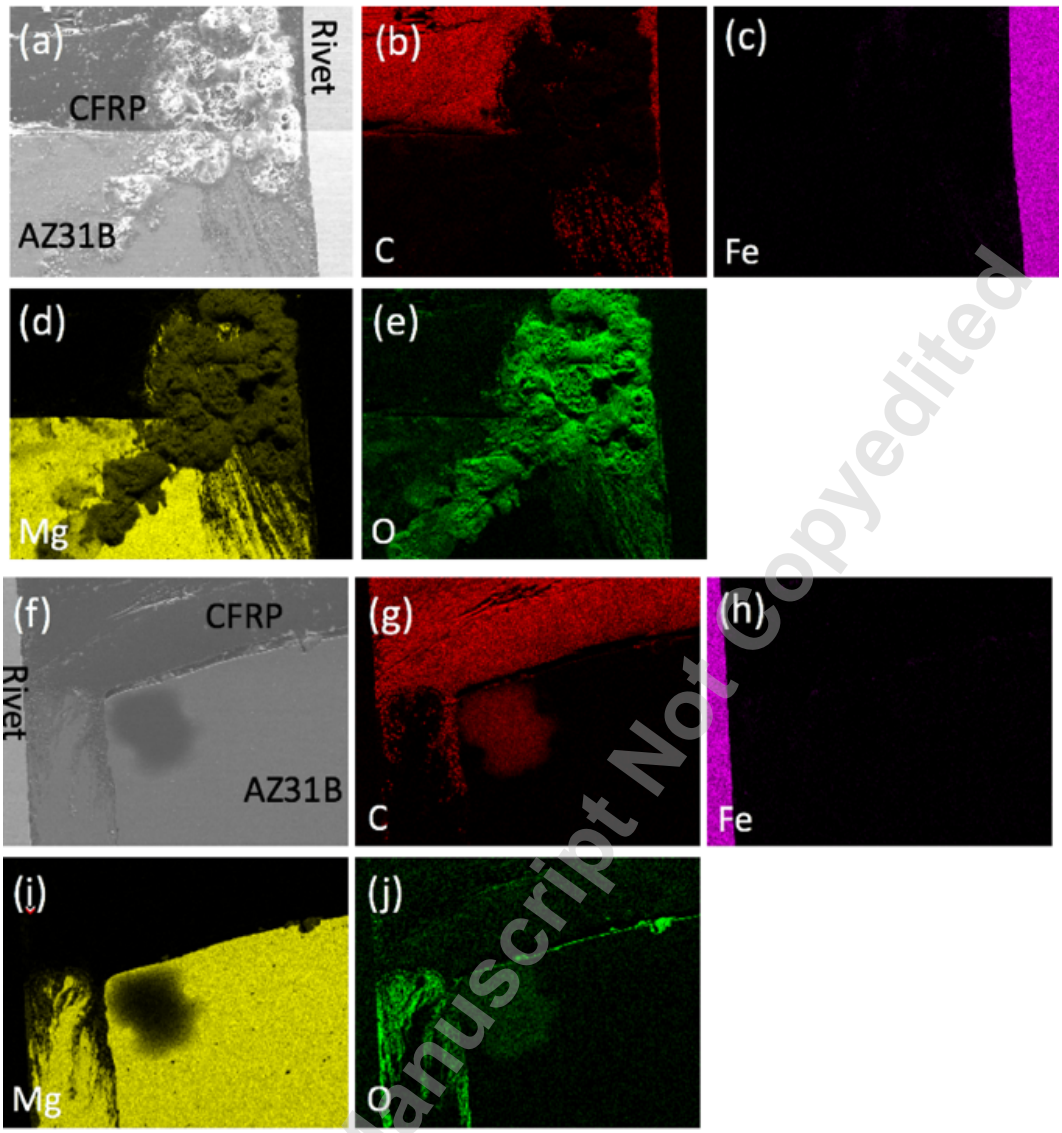

FIGURE 15. EDS mapping at F-SPR joint interface: left side joint interface (a–e); right side joint interface (f–j).

Journal of Manufacturing Science and Engineering. Received May 18, 2020;
Accepted manuscript posted May 20, 2020. doi:10.1115/1.4048378

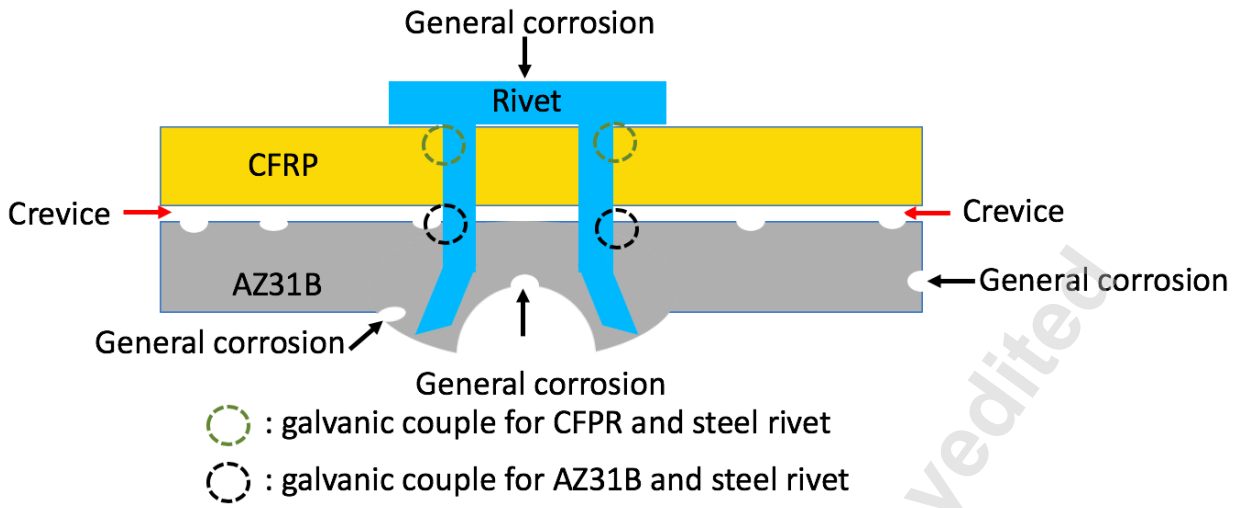

FIGURE 16. Schematic of F-SPR joint with potential corrosion mechanisms, including general, crevice and galvanic corrosion.